

Chapter 14

An Advanced Multi-Sectional Method for Particulate Matter Modeling in Flames

Andrea D'Anna and Mariano Sirignano

Abstract An advanced multi-sectional approach for modeling the gas-to-particle process in flames is presented. It follows the chemical evolution and the internal structure of particles formed in flames, fully coupled with the main pyrolysis and oxidation of the fuel. The multi-sectional method is included in a detailed mechanism of hydrocarbon pyrolysis and oxidation which considers the detailed formation of important gaseous species such as acetylene, benzene, and polycyclic aromatic hydrocarbons (PAHs); the lumped molecular growth of aromatics and particle inception; and the lumped particle growth and oxidation. The complete model is tested without any adjustments to the scheme on premixed and non-premixed flames of various hydrocarbons at atmospheric pressure. Predictions are compared with experimental data on gas-phase species concentrations, particle volume fractions, H/C and sizes in laminar premixed and in co-flowing non-premixed flames.

14.1 From Experimental Evidence to Model Development

Our understanding of soot formation has evolved from a phenomenological description to almost quantitative modeling in the last 10 years due to the progress of diagnostic tools, which today allow analysis on an almost atomic level of the particles, either offline or in situ (see [Chaps. 12](#) and [13](#)). Their use has improved our knowledge about the physical and chemical properties of combustion-formed particles and also about the kinetics of particle formation in combustion environments.

A. D'Anna (✉) · M. Sirignano
Dipartimento di Ingegneria Chimica, dei Materiali e della Produzione Industriale,
Università degli Studi di Napoli Federico II, Piazzale Tecchio 80 80125 Naples, Italy
e-mail: anddanna@unina.it

A broad range of particles with dimensions ranging from molecular size to some hundreds of nanometers are formed in combustion. The “molecular” particles behave spectroscopically as polycyclic aromatic hydrocarbons (PAH) absorbing UV light and showing an intense broadband fluorescence when excited with lasers in the UV. At the same time, they interfere with the laser light giving rise to more scattering than gas-phase compounds, thus indicating that they have a cross-section larger than gases and are thus typical of condensed phases. This class of particles is often referred to as nanoparticle of organic carbon (NOC) or visible-transparent nanoparticles (D'Anna 2009a).

As the size increases a solid-state character clearly appears. Larger particles emit thermal radiation once heated-up by an intense laser pulse and absorb light from UV to the visible range. A continuous transformation of the smaller particles through coagulation, dehydrogenation, and surface addition of gas-phase molecules—acetylene and PAHs—into larger particles leads to the formation of primary soot particles, with sizes from 10 to 40 nm, and soot aggregates whose size can reach values as high as 1 μm .

Chemical and spectroscopic characterization of the particles coupled with morphological studies revealed that ordered and disordered structures coexist in the soot particles (see Chap. 13). The order arises due to stacking of planar polycyclic aromatic hydrocarbons (PAHs) to form parallel atomic layers; the disordered part is due to the presence of randomly oriented and/or nonplanar PAHs. The combustion environment in which the particles are formed determines the final concentration of the particles as well as their organization on an atomic scale. Low temperatures, short residence times, and relatively low concentration of PAHs in the flame favor the formation of particles with disordered structures. Higher temperatures, longer residence times, and relatively high concentration of PAHs favor the formation of ordered structures with wide regions containing parallel stacks of PAHs (Alfè et al. 2009; Russo et al. 2013).

A number of detailed chemical mechanisms of PAH formation have been proposed to study PAH growth in flame environments. Kinetic mechanisms are based on the reactions of the abundant gaseous species such as C_2H_2 and small aromatic compounds activated by H and OH radicals. Along with the chemical growth reactions, the simultaneous physical process of coagulation of PAHs to form particle nuclei is considered. The presence of PAH stacks in experimental images of soot particles obtained by high-resolution transmission electron microscopy (HR-TEM) is proof of the coagulation of PAHs.

Particle nuclei can continue to add molecules to increase their sizes or they can coagulate with other particles maintaining an invariant total mass. Two different kinds of coagulation can be considered: coalescence and agglomeration. Coalescence occurs when a molecule from the gas-phase or a small particle collides with a particle and the formed entity tends to reduce free surface to minimize free energy. It results in the inclusion of the colliding molecules or small particles into the larger ones. In larger particles, the timescale of particle inclusion into the particle is larger than the timescale of the agglomeration process. In that case the

colliding entities maintain their own structure and they aggregate to form an agglomerate of particles.

Although the coagulation process (as sum of coalescence and agglomeration) has been widely observed for large PAH molecules and for small particles, their rates and the exact pathways in which they occur are still debated. The ability of PAHs to coagulate depends on dispersion forces. Planar pericondensed aromatic molecules have a high tendency to coagulate; the higher the molecular mass, that is, the number of aromatic cycles in the molecule, the higher the binding energy. Nonplanar aromatic molecules show a different behavior. They exhibit lower binding energies also at high-molecular mass because of the steric conformation of the molecules, which hinders the molecules from reaching an interaction distance. Therefore, the chemical structure of the PAHs and their sizes are controlling factors in determining the rate of particle inception and the internal structure of the incipient particles. The coagulation of planar pericondensed PAH might be responsible for the formation of ordered stacks of aromatics, whereas the coagulation of nonplanar aromatics results in less ordered clusters. PAH coagulation and addition of gas-phase compounds on the particle surface lead to particulate loading.

Parallel to the mechanisms which determine the increase of the particle size, that is, growth and agglomeration mechanisms, reaction of the particles with O₂ and OH may occur through two parallel processes: oxidation and fragmentation. Oxidation is the removal of mass from particles due to chemical reactions by hydroxyl radical and oxygen molecule. Fragmentation is the break-up of single particles and large aggregates into smaller particles and aggregates. Recent results by Sarofim's group (Echavarria et al. 2011) have confirmed the importance of oxidation-induced fragmentation in correctly determining the burn-out rate of particles. The reactions of the fragmentation process have been recently included by Pitsch's group in their model to predict particle size distribution in premixed flames (Mueller et al. 2011). However, in that model only the fragmentation of aggregates has been considered.

Fragmentation can involve large aggregates containing a large number of primary particles. Stepwise splitting up of large aggregates for effect of oxidation-induced fragmentation can lead to smaller aggregates formed by just two primary particles. In this case a subsequent fragmentation forms isolated primary particles. Fragmentation can also involve primary particles. In this case internal burning fragments single particles into smaller clusters. This process can continue producing very small cluster fragments.

Aggregate fragmentation and single-particle fragmentation are conceptually different. The fragmentation of aggregates into smaller aggregates of primary particles is mainly linked with the presence of material condensed from the gas-phase or added to the particle by surface reactions which fill the space between the particle contact points. The fragmentation of particles into smaller particles deals with the internal structure of the single particles.

Based on the above considerations, a detailed mechanism of particle evolution is proposed to delve into the physical structure and chemistry of combustion-

formed particles. A multi-sectional method is used with a triple discretization of the particle phase in terms of C and H atom number, and morphology. This allows following not only the mass of particles, but also the hydrogen content and internal structure. This description of the particles improves the treatment of the inception and growth pathways by coupling their kinetics to features such as H/C ratio or morphology, following the hints suggested by the experimental evidences. In particular, modeling of the detailed structures of the particles allows the inclusion of oxidation pathways by OH and O₂, surface reactions, and O₂ induced fragmentation.

The model follows the chemical and internal structure evolution of particles formed in flames. Other sophisticated approaches are currently used to simulate internal structures of the particles (see [Chap. 15](#)). The model presented here is fully coupled with the main pyrolysis and oxidation reactions of the fuel. The coupling between gas and particle phase is important because of the role of abundant gaseous species such as C₂H₂, aromatic compounds and small radicals such as H and OH in the nucleation, growth, and oxidation processes.

The model is tested, without any adjustments to the scheme, on premixed and non-premixed flames of ethylene at atmospheric pressure. Predictions are compared with experimental data on gas-phase species concentrations, particle volume fractions, H/C and size in laminar, premixed, and in co-flowing non-premixed flames.

Hereafter the model will be presented in detail. First of all, the gas-phase reactions will be briefly described. Successively, the sectional method will be introduced and details on the multi-sectional approach and discretizations adopted will be given. Finally, the different processes for particle evolution and the reaction used for modeling them, molecular growth, gas-to-particle transition, oxidation, and oxidation-induced fragmentation, will be described.

14.2 Gas-Phase Chemistry and PAH Formation

The mechanism of oxidation and pyrolysis of small aliphatic hydrocarbons is built onto the GRI-Mech 3.0 for C1 and C2 species (Smith et al. [2013](#)) and the Miller and Melius mechanism for C3 and C4 species (Miller and Melius [1992](#)). It has been used to model several flame conditions at atmospheric pressure showing reasonable ability to predict the structures of aliphatic and aromatic hydrocarbon flames (D'Anna [2009b](#)).

Briefly, fuel-rich conditions promote molecular growth and hydrogen loss and also oxidation of the hydrocarbon molecules. In aliphatic fuel flames, acetylene and methane are the most abundant, gaseous, unburned hydrocarbons and benzene is the first aromatic product of the molecular growth process. Benzene formation is considered to occur by the addition of *n*-C4 radicals to C₂H₂ and the self-combination of propargyl radicals (C3-route). The sequential addition of C₂H₂ to phenyl radical (hydrogen abstraction acetylene addition—or HACA—mechanism,

Frenklach and Wang (1991, 1994) and the combination of resonantly stabilized radicals, that is, the combination of two cyclopentadienyl radicals and the combination of benzyl and propargyl radicals (Marinov et al. 1996), are the pathways considered for the growth of aromatic cycles up to pyrene. Since the combustion conditions can be quite different in terms of gas-phase species concentration and temperature history, very often some extreme conditions have been analyzed drawing generally valid conclusions. As for other steps in particle formation, it is very likely that these mechanisms march together and just in some case one is completely prevalent with respect to the other.

Pyrene is considered to be the largest possible gas-phase compound. All species with larger molecular weight are treated as lumped species and thus divided into classes. The gas-phase kinetic mechanism consists of 460 reactions involving 120 species.

14.3 Advanced Multi-Sectional Approach

Compounds with molecular weight larger than pyrene become very difficult to model due to their large number of isomers. Many approaches have been proposed through years.

Some methods have risen as the most efficient for soot prediction. Sectional approach, that is, discretization of the molecular mass of the species leading to soot, is one of the possible solutions to the particle population balance problem. In fact, to solve the population balance problem when an analytical solution is not possible, probably the first approach is to discretize the domain and try to get an approximate solution. The limit of this approach would be the use of an infinite number of sections to get the continuous solution. It uses lumped species in order to incorporate particle dynamics. Particles are divided into classes, but each one is treated as a gas-phase so that elemental reaction steps can then be written. This allows to account for a lot of chemical details of reaction steps which would otherwise be lost.

This method allowed in the beginning to have information on total amount of soot and particle size distribution, since the first discretization was made on the carbon atoms contained in each lumped species, that is, the mass of the particle. This first version has been developed by several groups and tested in many flame configurations for different fuels (Smooke et al. 1999; Richter et al. 2005; D'Anna and Kent 2008; Mauss et al. 2009; Dworkin et al. 2011). The advanced multi-sectional method (AMS) for particle description in flames presented here is the latest development in the discrete sectional approach (Sirignano et al. 2010; D'Anna et al. 2010).

The use of lumped species treats, numerically, all the particles as gas-phase species. This means that it is possible to evaluate a collision frequency and to assign an activation energy for each process in which particles are involved. The kinetic expression can be written in principle for each lumped species. Particles

react in a similar way, depending on some parameters, such as size, chemical composition, and morphology. Kinetic expressions will be tailored on particle features, assuming specific dependence on these parameters. If these dependences are chosen on the basis of physical meanings their validity can be wider. This approach tries to get more general expressions for particle reaction avoiding the tuning of kinetic rates for matching experimental data.

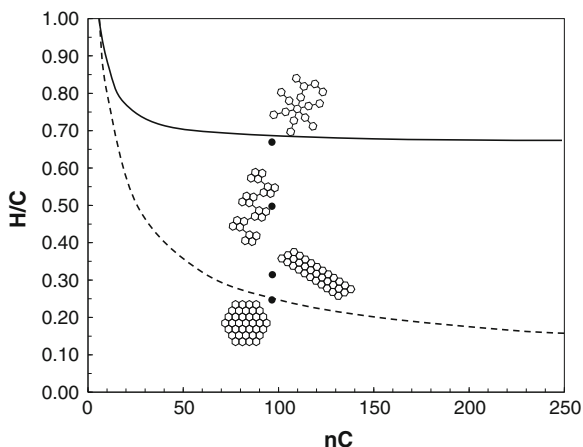
The molecular mass distribution is defined by a range of sections, each containing a nominal hydrocarbon species in order of increasing atomic mass. Carbon number ranges from 24 to 2×10^{10} and H/C for each carbon number ranges from 0 to 1. Thirty-one sections are used in a geometric series of carbon number with a ratio of two between sections. Five sections are used for H/C variation. The model introduces another discretization which accounts for the level of agglomeration of the compounds. Three entities are defined: molecules (ARM1i), clusters of molecules (ARM2i), and agglomerates of clusters (ARM3i). The index *i* represents the discrete sections in which the C-atom domain has been divided (31 sections), whereas the H atom content is taken into account by considering five different lumped species having the same number of C-atoms and different numbers of H atoms. Overall, 465 lumped species for the stable form and 465 for radicals are modeled. It is assumed that only one radical species is representative of each stable species. The equivalent size range of 1–800 nm is obtained with this discretization considering a density varying from 1 g/cm³ for the smallest species with the highest hydrogen content to 1.8 g/cm³ for species above 10 nm with the lowest hydrogen content.

14.3.1 Particle Phase Reaction: Gas-to-Particle Transition

The discretization operated for the lumped species furnishes a rough estimation of their molecular structure. Experimental evidence indicates that high molecular mass species generated in flames are essentially aromatic compounds (Homann 1998). So, for a given C-atom number, molecules with large H/C ratios must be aromatics having both σ - and π -bonds between C-atoms consisting of incompletely condensed oligomers of aromatics, whereas lower H/C molecules belong to the class of the maximally condensed aromatics hydrocarbons, that is, pericondensed aromatic compounds (PCAHs), in which only π -bonds among C exist. Figure 14.1 shows the H/C as a function of the number of C-atoms up to 250 for the oligomers of benzene (high H/C values—full line) and that of maximally condensed aromatics (low H/C values—dashed line). In the figure, an example of an aromatic molecule having 96 C-atoms and different H atom numbers is also shown.

Starting from pyrene, the molecular growth of aromatics is initiated by an H atom loss (R1, R2, and R3) from aromatic molecules ARM1i forming an aromatic radical ARM1i* (Table 14.1). For the H-abstraction reaction by H (R1) or OH (R2), the collision frequency evaluated by kinetic theory indicates a dependence

Fig. 14.1 H/C as a function of the number of C-atoms up to 250 for the oligomers of benzene (high H/C values—*full line*) and that of maximally condensed aromatics (low H/C values—*dashed line*). An example of the aromatic molecules having 96 C-atoms and different H atom numbers is also shown



on carbon atoms raised to the $2/3$ power. The effective possibility that the contact of H and OH radical produces an H-abstraction depends on H availability. Consequently, the reaction rate is scaled by the H/C of the particles. The reverse reaction rates are based on the similarity with PAHs of increasing mass; they depend on mass and H/C. Activation energies are made equal to those of H-abstraction from a benzenic ring in gas-phase PAHs (Frenklach and Wang 1994).

The spontaneous formation of radicals (R3) is built on the similarity with the naphthalene reaction. It is a unimolecular reaction. The reaction rate increases with an increase in the number of hydrogen atoms in the molecules (Richter et al. 2005).

Termination reactions of aromatic radicals with other aromatic radicals (R4) ending the growth sequence have rate constants evaluated from the collision frequencies of the reacting species. A collision between two molecules with differing number of carbon atoms scales with mean number to the $1/6$ power; it is considered to have zero activation energy (Frenklach and Wang 1994).

The formation of PCAHs is modeled by addition of acetylene (R5) (Frenklach and Wang 1994). The rate constant for acetylene addition to aromatic radicals (R5) is based on the reaction rate of naphthyl + acetylene scaled by increasing collision frequencies (Richter et al. 2005). PCAHs with a fixed number of C-atoms exist in a large number of isomers having different H atoms. The PCAHs having the lowest amount of H atoms are maximally condensed six-member ring structures. Their H/C ratio decreases to very low values as the molecular size increases; the largest of these compounds is a graphene sheet.

The formation of incompletely condensed aromatics is modeled both by H atom substitutions by a pericondensed structure, e.g., the formation of phenyl-pyrene or naphthyl-pyrene, and by aromatic radical addition to non-aromatic double bonds, such as those of pentagons condensed peripherally with hexagons (acenaphthylene type), and those of compounds like phenanthrene (R6). On the basis of structural

Table 14.1 Lumped species mechanism. Units are cal, mole, cm, s

Reactions	$k = AT^n \exp[-E/RT](nC)^p (H/C)^q$
<i>Molecules</i>	
R1	$ARM1i + H \leftrightarrow ARM1i^* + H_2$ $8.85E13 T^{0.5} \exp(-16,000/RT) nC^{2/3} H/C$
R2	$ARM1i + OH \leftrightarrow ARM1i^* + H_2O$ $8.85E13 T^{0.5} \exp(-4,650/RT) nC^{2/3} H/C$
R3	$ARM1i \rightarrow ARM1i^* + H$ $6.00E14 T^{0.5} \exp(-113,100/RT) nC H/C$
R4	$ARM1i^* + ARM1i^* \rightarrow ARM1i$ $8.00E12 T^{0.5} nC^{1/6}$
R5	$ARM1i^* + C_2H_2 \rightarrow ARM1i$ $3.00E6 T^{1.787} \exp(-3,262/RT) nC^{0.616}$
R6	$ARM1i^* + ARM1i \rightarrow ARM1i + H$ $2.00E13 T^{0.5} \exp(-15,000/RT) nC^{1/6}$
R7	$ARM1i + H \rightarrow ARM1i + H + H_2$ $6.00E14 T^{0.5} \exp(-25,000/RT) nC H/C$
R8	$ARM1i + OH \rightarrow ARM1i + HCO$ $3.00E12 T^{0.5} \exp(-10,600/RT) nC^{0.623}$
R9	$ARM1i^* + O_2 \rightarrow ARM1i + 2CO$ $4.30E11 T^{0.5} \exp(-8,000/RT) nC^{2/3}$
R10	$ARM1i + ARM1i \rightarrow ARM2i$ $\gamma 8.00E12 T^{0.5} nC^{1/6}$
<i>Clusters</i>	
R11	$ARM2i + H \leftrightarrow ARM2i^* + H_2$ $8.85E13 T^{0.5} \exp(-16,000/RT) nC^{2/3} H/C$
R12	$ARM2i + OH \leftrightarrow ARM2i^* + H_2O$ $8.85E13 T^{0.5} \exp(-4,650/RT) nC^{2/3} H/C$
R13	$ARM2i \rightarrow ARM2i^* + H$ $6.00E14 T^{0.5} \exp(-113,100/RT) nC H/C$
R14	$ARM2i^* + ARM1i^* \rightarrow ARM2i$ $8.00E12 T^{0.5} nC^{1/6}$
R14	$ARM2i^* + ARM2i^* \rightarrow ARM2i$ $8.00E12 T^{0.5} nC^{1/6}$
R15	$ARM2i^* + C_2H_2 \rightarrow ARM2i$ $3.00E6 T^{1.787} \exp(-3,262/RT) nC^{0.616}$
R16	$ARM2i^* + ARM2i \rightarrow ARM2i + H$ $2.00E13 T^{0.5} \exp(-15,000/RT) nC^{1/6}$
R16	$ARM2i^* + ARM1i \rightarrow ARM2i + H$ $2.00E13 T^{0.5} \exp(-15,000/RT) nC^{1/6}$
R16	$ARM1i^* + ARM2i \rightarrow ARM2i + H$ $2.00E13 T^{0.5} \exp(-15,000/RT) nC^{1/6}$
R17	$ARM2i + H \rightarrow ARM2i + H + H_2$ $6.00E14 T^{0.5} \exp(-25,000/RT) nC H/C$
R18	$ARM2i + OH \rightarrow ARM2i + HCO$ $3.00E12 T^{0.5} \exp(-10,600/RT) nC^{0.623}$
R19	$ARM2i^* + O_2 \rightarrow ARM2i + 2CO$ $4.30E11 T^{0.5} \exp(-8,000/RT) nC^{2/3}$
R20	$ARM1i + ARM2i \rightarrow ARM2i$ $\gamma 8.00E12 T^{0.5} nC^{1/6}$
R20	$ARM2i + ARM2i \rightarrow ARM2i$ $\gamma 8.00E12 T^{0.5} nC^{1/6}$
R21	$ARM2i + ARM2i \rightarrow ARM3i$ $\gamma 8.00E12 T^{0.5} nC^{1/6}$
R22	$ARM2i^* + O_2 \rightarrow ARM2i + ARM2i + 2CO$ $\beta 1.72E9 T^{0.5} \exp(-8,000/RT) nC^{5/3}$
<i>Agglomerates</i>	
R23	$ARM3i + H \leftrightarrow ARM3i^* + H_2$ $8.85E13 T^{0.5} \exp(-16,000/RT) nC^{2/3} H/C$
R24	$ARM3i + OH \leftrightarrow ARM3i^* + H_2O$ $8.85E13 T^{0.5} \exp(-4,650/RT) nC^{2/3} H/C$

(continued)

Table 14.1 (continued)

Reactions	$k = AT^n \exp[-E/RT](nC)^p (H/C)^q$
R25 ARM3i → ARM3i* + H	$6.00E14 T^{0.5} \exp(-113,100/RT) nC$ H/C
R26 ARM3i* + ARM1i* → ARM3i	$8.00E12 T^{0.5} nC^{1/6}$
R26 ARM3i* + ARM2i* → ARM3i	$8.00E12 T^{0.5} nC^{1/6}$
R26 ARM3i* + ARM3i* → ARM3i	$8.00E12 T^{0.5} nC^{1/6}$
R27 ARM3i* + C ₂ H ₂ → ARM3i	$3.00E6 T^{1.787} \exp(-3,262/RT)$ $nC^{0.616}$
R28 ARM3i* + ARM1i → ARM3i + H	$2.00E13 T^{0.5} \exp(-15,000/RT) nC^{1/6}$
R28 ARM3i* + ARM2i → ARM3i + H	$2.00E13 T^{0.5} \exp(-15,000/RT) nC^{1/6}$
R28 ARM3i* + ARM3i → ARM3i + H	$2.00E13 T^{0.5} \exp(-15,000/RT) nC^{1/6}$
R28 ARM3i + ARM1i* → ARM3i + H	$2.00E13 T^{0.5} \exp(-15,000/RT) nC^{1/6}$
R28 ARM3i + ARM2i* → ARM3i + H	$2.00E13 T^{0.5} \exp(-15,000/RT) nC^{1/6}$
R29 ARM3i + H → ARM3i + H + H ₂	$6.00E14 T^{0.5} \exp(-25,000/RT) nC$ H/ C
R30 ARM3i + OH → ARM3i + HCO	$3.00E12 T^{0.5} \exp(-10,600/RT) nC^{0.623}$
R31 ARM3i* + O ₂ → ARM3i + 2CO	$4.30E11 T^{0.5} \exp(-8,000/RT) nC^{2/3}$
R32 ARM3i + ARM3i → ARM3i	$\gamma 8.00E12 T^{0.5} nC^{1/6}$
R32 ARM1i + ARM3i → ARM3i	$\gamma 8.00E12 T^{0.5} nC^{1/6}$
R32 ARM2i + ARM3i → ARM3i	$\gamma 8.00E12 T^{0.5} nC^{1/6}$
R33 ARM3i* + O ₂ → ARM3i + ARM3i + 2CO	$\alpha 4.30E0 T^{0.5} \exp(-8,000/RT) nC^{5/3}$
R33 ARM3i* + O ₂ → ARM2i + ARM2i + 2CO	$\alpha 4.30E0 T^{0.5} \exp(-8,000/RT) nC^{5/3}$

nC is carbon number of the reactants except in reactions in which two lumped species are involved, where it represents average carbon number of the two reactants; H/C is the H-to-C ratio in the species; T is the flame temperature; R is the universal gas constant

similarity, the rate constant for phenyl + benzene is used as the reference for the corresponding aromatic radical + aromatic molecule reaction (R6) which is scaled for variation in collision frequencies (Richter et al. 2005).

The H/C ratio of the oligomers remains comparable to those of the aromatic molecules involved in the reactions and it remains quite unchanged as the molecular weight of the oligomers increases. Aromatic oligomers usually assume a nonplanar structure due to the less rigid structure of the σ -bond connecting the aromatic molecules.

Both pericondensed and incompletely condensed aromatics can grow indefinitely forming extremely large molecules. PCAHs can only add acetylene (R5) or other gaseous hydrocarbons (if an aromatic molecule is added an incompletely condensed aromatic is formed—R6). Incompletely condensed aromatics can also undergo dehydrogenation reactions migrating to pericondensed molecules (R7). The dehydrogenation has been considered occurring only on the stable species and not on radicals. The dehydrogenation process considers that, due to the complexity of the structures with increasing number of C-atoms, the radicals formed through the attack of an H atom cyclize forming a closed aromatic ring. The limiting stage is the rearranging of the structure to expel an H atom and form a new stable species with a lower H/C ratio, and consequently higher aromaticity. An activation energy

of 25,000 cal/mol has been estimated to better reproduce the experimental data (Sirignano et al. 2010). The dependence of the reaction rate on the number of H present in the structure is also considered.

The molecular growth process competes with molecule oxidation by OH and O₂ (R8 and R9). OH is used to oxidize the stable molecule, whereas O₂ oxidizes the radicals. The activation energy of the oxidation by OH (R8) is estimated from similar reactions for benzene and PAHs and the collision frequency accounts for the size of the particles involved (Neoh et al. 1985). Oxidation by O₂ (R9) uses the rate constant of naphthyl + O₂ accounting for the increase of collision frequencies of Xu et al. (2003).

Together with chemical growth, the physical process of PAH coagulation, that is, long-range interaction between colliding entities, occurs to form particle nuclei (R10). The current model introduces a further discretization which accounts for the formation of clusters of molecules (particle nuclei) here defined as ARM2i.

Clusters of molecules are stacks of PAHs held together by van der Waals interactions. Binding energies which form these clusters depend on the dimensions of the interacting aromatic molecules and on the capability of the aromatic molecules to reach an interaction distance. PCAHs which have an intrinsic planar structure due to the absence of σ -bonds can easily reach an interaction distance and arrange in parallel stacks. Structures which contain σ -bonds tend to assume a nonplanar structure so that the steric conformation of these molecules hinders π -electrons of the molecules reaching an interaction distance. This conformation is responsible for lower binding energies. Dehydrogenation of molecules leads to a more pericondensed structure, inducing planarity in the molecules and increasing the capability of the molecules to reach an interaction distance. As a consequence, coagulation of PAHs depends on molecule sizes, and on the number of π -bonds with respect to σ -bonds. Molecule size is accounted for through the number of C atoms, whereas the H/C accounts for the number of π - and σ -bonds. For the same C atom number, high H/C means σ -bond interactions in the molecule, nonplanar structure, and hence lower coagulation rate. On the other hand, low H/C means mainly π -bond interactions in the molecule, intrinsic planar structure, and hence higher coagulation rate.

Molecule coagulation (R10) is considered irreversible at this stage and its reaction rate is modeled by considering a coagulation efficiency with respect to the collision frequency. Collision frequency increases with the increase of molecular mass of the molecules, whereas the coagulation efficiency, γ , depends on both the temperature and chemistry of the colliding molecules. The chemistry of the particles is considered by evaluating the Hamaker constant (Hamaker 1937) for the species involved in the coagulation process. The Hamaker constant accounts for van der Waals body-body interactions. From benzenic ring to graphite the Hamaker constant ranges from 3×10^{-20} to 5×10^{-19} J.

A value of 5×10^{-20} J has been assigned to a compound with an H/C ratio of 0.5. The values of the Hamaker constant for the other compounds have been linearly scaled on the H/C ratio. The coagulation efficiency is evaluated by following D'Alessio et al. (2005): $\gamma = 1 - (1 + \Phi_0/T) \exp[-\Phi_0/T]$ evaluated as a

function of the flame temperature T , and the interaction potential Φ_0 between coagulating entities. The latter is a linear function of the Hamaker constant (Sirignano et al. 2010).

The computed coagulation efficiency is of the order of 10^{-4} for small colliding entities and increases to values of about 1 when the C number is about 10^6 . These values are in agreement with experimental coagulation rates (D'Alessio et al. 2005). The modeled results show that high H/C molecules, that is, mostly comprising incompletely condensed aromatics and hence nonplanar compounds, have much lower coagulation efficiencies than low H/C molecules, that is, planar pericondensed aromatic compounds, for the same number of C-atoms.

14.3.2 Particle Phase Reaction: Particle Growth Mechanism

Clusters of molecules, that is, particle nuclei, (ARM2i) can continue to react in the same way as the molecules (ARM1i). Table 14.1 reports the list of reactions involving ARM2i compounds. They can add molecules to increase their size (R11–R16), or remove H atoms by dehydrogenation (R17) or C atoms by OH and O₂ oxidation (R18 and R19), or they can coagulate with other molecules or other clusters (R20). If two clusters merge into one reducing free surface area so as to minimize their free energy a coalescence event occurs (R20). The formed cluster assumes a spherical shape and can be seen as a cluster of molecules larger than the previous two (Fig. 14.2).

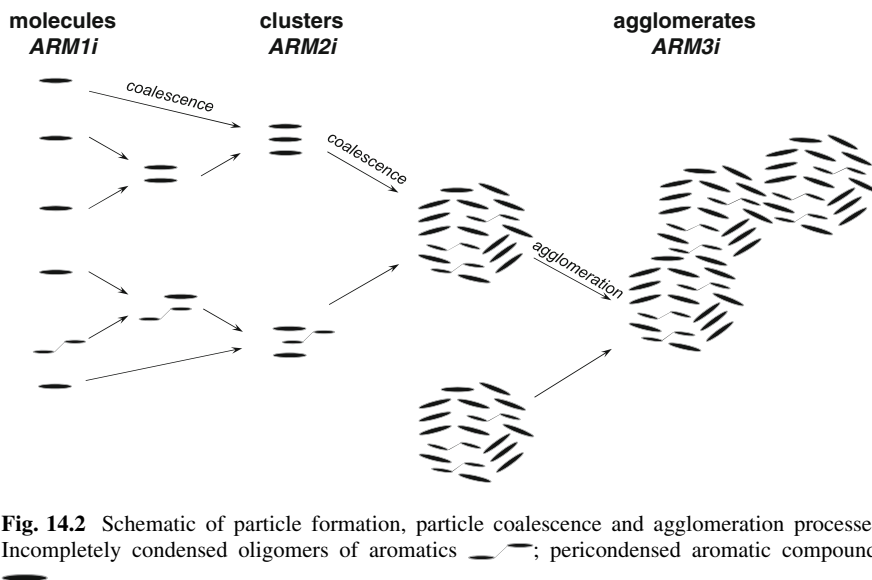


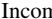

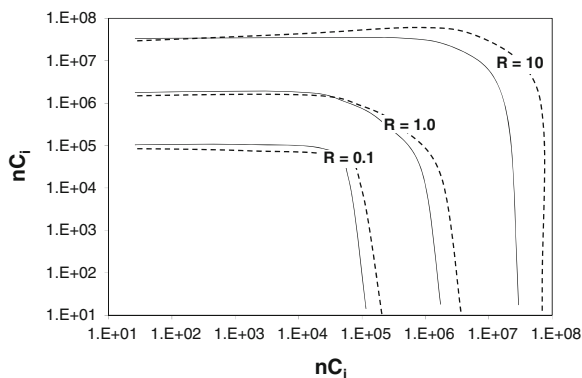
Fig. 14.2 Schematic of particle formation, particle coalescence and agglomeration processes. Incompletely condensed oligomers of aromatics ; pericondensed aromatic compounds 

Fig. 14.3 Ratio (R) of agglomeration/coalescence rates at 1800 K for low ($H/C < 0.25$ —full lines) and high ($H/C > 0.25$ —dashed lines) species



As the cluster size increases, the timescale of molecular coalescence becomes larger than the timescale of the agglomeration process, and consequently the coagulation events lead to the formation of agglomerates (R21). Figure 14.3 shows contours of the ratio of the agglomeration to coalescence regimes at 1800 K for low (lower than 0.25—full lines) and high (larger than 0.25—dashed lines) H/C species.

It appears that particles with an nC of 1×10^5 (equivalent size of about 10 nm) have a rate of coalescence higher than that of agglomeration. This behavior is reversed for structures with nC larger than 1×10^6 (equivalent size of about 20 nm). For particles of 10–20 nm, coalescence and agglomeration rates are similar which means that these particles can coalesce or agglomerate with the same probability. Sensitivity analyses have been conducted by changing the size and H/C ratio dependence of the coalescence rate. The coalescence–agglomeration ratio does not drastically affect the final concentration of the particles but it does determine the size of the primary particles which constitutes particle agglomerates.

Particle agglomerates (ARM3i) can undergo the same reactions as the clusters of molecules (ARM2i) and the single molecules (ARM1i) (R23–R32).

14.3.3 Particle Phase Reaction: Oxidation-Induced Fragmentation

Particles oxidation is generally considered a surface process through which carbon atoms are subtracted from the particles. If the oxidizing species are able to remove C-atoms near a contact point between two particles constituting an aggregate or even penetrate the pores internally oxidizing the particle, the break-up of the large aggregates and particles into smaller aggregates and particles can occur. These processes can be referred to as oxidation-induced fragmentation and can be seen as particular events of oxidation. Aggregate fragmentation (R33) and single particle fragmentation (R22) are both considered in the model.

The aggregates are fragmented when oxidation occurs at the contact points of the primary particles after the removal of a fraction δ of C atoms from the particles. This consideration is linked to the consideration that there is more than one pair of carbon atoms holding together the aggregate. The points of weakness are the contact points between the particles and the number of contact points in the aggregates is given by $(n_p - 1)$, where n_p is the number of primary particles in the aggregate that can be calculated as $n_p = n_{C_A}/n_{C_P}$, being n_{C_A} and n_{C_P} the number of C atoms in the aggregate and in the primary particle, respectively.

The probability that the oxidation occurs in a weakness point between two particles is equal to the inverse of the number of active sites on the particle surface for O_2 oxidation:

$$n_{\text{active sites}} = \chi \times \pi \times d_p^2$$

where χ is the number of sites per unit area ($\chi = 1.7 \times 10^{19} \cdot \text{m}^{-2}$ was estimated by Kazakov and Frenklach 1998), d_p is the particle size, and πd_p^2 is the primary particle surface area. Each oxidation event removes two carbon atoms (R31). To have an oxidation event which is able to activate fragmentation, a fraction δC of atoms has to be removed. The number of C atoms that must be removed to cause fragmentation can be expressed as follows:

$$\delta C = \alpha \times n_{C_P}$$

where α is a fraction of the C atoms constituting the primary particles.

The fragmentation rate of aggregates (R32) is then given by:

$$k_f = k_{O_2} \times (n_p - 1) / ((\chi \times \pi d_p^2) \times \delta C)$$

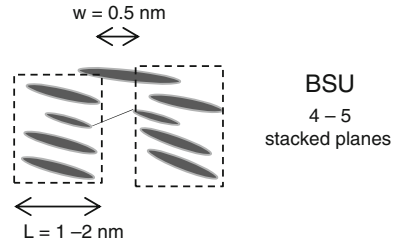
where k_{O_2} is the rate constant of the oxidation reaction.

The fragmentation of agglomerates with n_C lower than 1×10^6 is considered to form clusters of molecules (primary particles) (R33).

A similar approach is used to model fragmentation of particles into smaller particles (R22). Experimental data obtained by HR-TEM on incipient particles (Alfè et al. 2009) show that particles appear to be composed of clusters of aromatic compounds. Generally, the average molecular mass of the aromatic compounds included in a cluster is such that its length in the HR-TEM images is of the order of 1 nm which corresponds to compounds having about 20–25 C atoms. The number of aromatics in well-organized structures is always of the order of 4–5 stacked planes at a distance of about 0.35 nm. As a consequence, organized structures in an incipient particle, often referred to as basic structure units (BSUs), can be schematized as cylindrical units having equal base diameter and length of about 1 nm. These BSUs are randomly organized in the particles and are separated from each other by “pores” having a length of the same order of magnitude of the BSU and size of about 0.5 nm. Figure 14.4 shows a schematic representation of the BSUs inside the particle.

Molecular oxygen oxidizes a particle on its surface but it can also penetrate the pores internally oxidizing the particle. The calculated effective diffusivity time of

Fig. 14.4 Schematic representation of two BSUs



O_2 molecule inside the pores separating the BSUs is lower than the characteristic time of surface oxidation leading to the hypothesis that diffusivity of O_2 is not the controlling step in the internal oxidation of particles. On the other hand, because of the fast reactivity of OH oxidation, the OH radical does not penetrate the pores but oxidizes the particle on its surface.

When oxidation by O_2 occurs in the depth of the pores, the particle can fragment into two parts by the removal of δC -atoms. The number of C atoms in the BSU, $n_{C_{BSU}}$, is estimated by considering the BSU made up of 4 aromatic molecules each of 25 C atoms, on the basis of HR-TEM images. The number of BSUs constituting a particle, n_{BSU} , is obtained by dividing the number of C atoms in the particle by the number of C atoms constituting the BSU, $n_{BSU} = n_{C_p}/n_{C_{BSU}}$. The number of pores, n_{pores} , can be evaluated from the volume of a single pore relative to the particle volume. For cylindrical pores with a depth L , of the same order of magnitude of the BSU (1 nm) and diameter, w , of about 0.5 nm, the internal surface of the pores is $(\pi w L + \pi w^2/4)$. However, the point of weakness in the pore is considered to be at the bottom and so only this fraction of pore area is used $(\pi w^2/4)/(\pi w L + \pi w^2/4)$.

The particle fragmentation rate (R22) is related to the O_2 oxidation rate— k_{O_2} —by evaluating the probability that the oxidation occurs at the bottom of the pores after removal δC -atoms as discussed above. This number of carbon atoms is given here by

$$\delta C_{pores} = \beta \times n_{C_p}$$

where β represents the fraction of C atoms in the particle that must be removed to cause fragmentation.

The fragmentation rate for the particles (R22) is then:

$$k_f = k_{O_2} \times (\pi w^2/4 / (\pi w L + \pi w^2/4)) \times n_{pores} / (\delta C_{pores})$$

Values of $\alpha = 0.01$ and $\beta = 0.05$ give the best agreement of the modeled results with the experimental data of Echavarria et al. in premixed flames (Echavarria et al. 2011). The impact of these processes on the final soot burn-out and size distribution will be shown below.

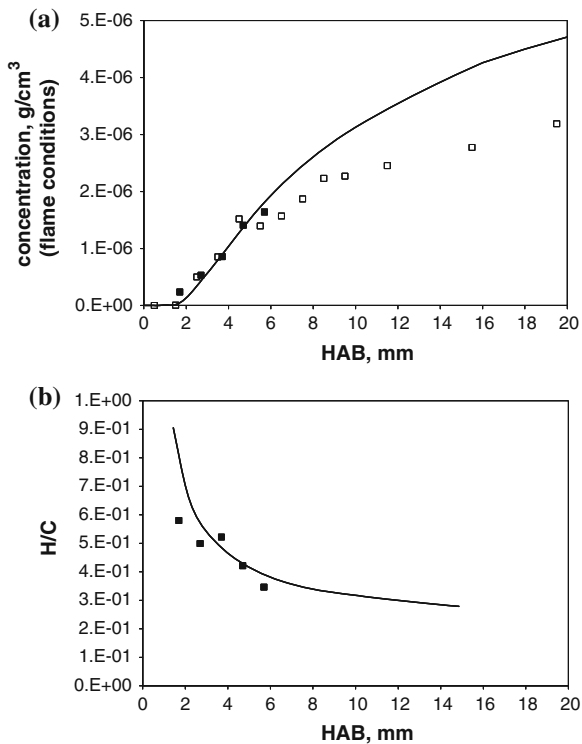
14.4 Use of the Advanced Multi-Sectional Method in Combustion Systems

14.4.1 Laminar Premixed Flames: Test Cases

The model is applied to sooting premixed flames of ethylene at atmospheric pressure (Ciajolo et al. 1996, 1998; Sgro et al. 2009). Different diagnostics have been used for their characterization. They furnish details of flame structures, particle concentrations, their size distribution functions, and the chemical structure and molecular mass of the condensed phases.

Figure 14.5 shows the comparison of the model to the experimentally determined concentration of total particulates and H/C ratio in the rich ethylene/oxygen premixed flames with equivalence ratio $\phi = 2.4$. The measured flame temperature profile is needed as an input to the model for a correct simulation of the flame structure. Modeled total particulate is here defined in agreement with experiment, as the mass of all compounds with a number of C-atoms higher than 10 (molecular mass equal or larger than naphthalene). Particulate concentration increases just downstream of the maximum flame temperature—located at about 2 mm height

Fig. 14.5 Comparison of the model (*lines*) to the experimentally determined concentrations (*points*) of (a) total particulate—the species with molecular mass equal or larger than naphthalene—and (b) its H/C ratio in the $\phi = 2.4$ ethylene/oxygen premixed flames at atmospheric pressure. Experimental data from Ciajolo et al. 1996 (\square) and 1998 (\blacksquare) (D’Anna et al. 2010, Copyright Elsevier)



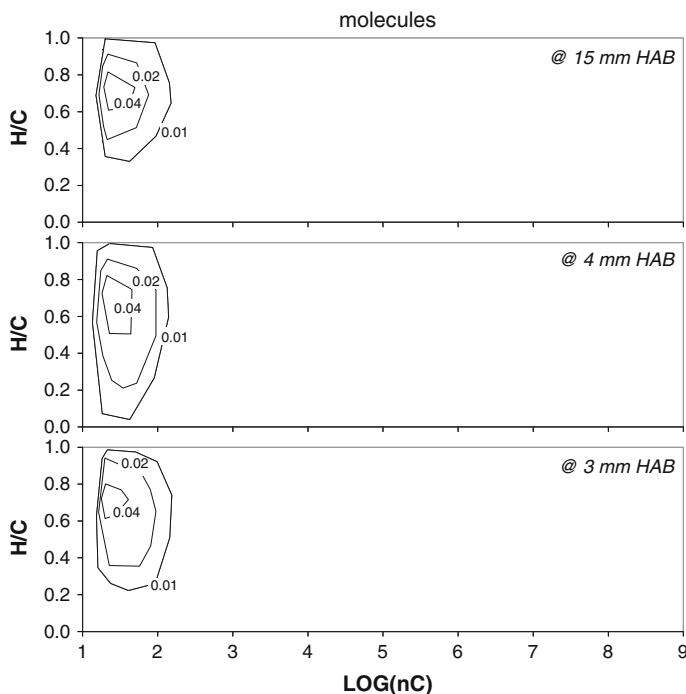


Fig. 14.6 Modeled H/C ratio distribution of molecules as a function of the C-atom numbers (nC) at three heights in the $\phi = 2.4$ flame. From *bottom* to *top*: 3, 4, and 15 mm. Lines are iso-concentrations in part per million (D'Anna et al. 2010, Copyright Elsevier)

above burner, HAB—at a fast rate and thereafter it levels off. By contrast, the H/C ratio decreases monotonically with increasing flame height. The model predicts the experimental data reasonably well and particularly it captures the increase in concentration of total particulates and the decrease in hydrogen content.

Figures 14.6, 14.7, and 14.8 show modeled H/C ratio distribution of the high-mass compounds against number of C-atoms at three heights in the $\phi = 2.4$ flame, namely at particle inception (3 mm), at the location where particle formation rate is maximum (4 mm), and in the post-flame region (15 mm). The predictions are for molecules (Fig. 14.6), clusters (Fig. 14.7), and agglomerates (Fig. 14.8).

The model indicates that molecules of aromatic hydrocarbons are formed at particle inception which occurs just downstream of the flame front. Their H/C ratio extends over a wide range of values, whereas their C-atom numbers do not exceed 100. The species with the largest concentrations have about 20–40 carbon atoms and H/C ranging from 0.6 to 0.8. The H/C of these compounds suggests that they comprise pericondensed and incompletely condensed PAHs.

Moving downstream into the main flame region the mass of single molecules remains quite unchanged and their H/C is reduced. These changes indicate a larger presence of pericondensed PAHs in the molecule pool. It occurs at the height

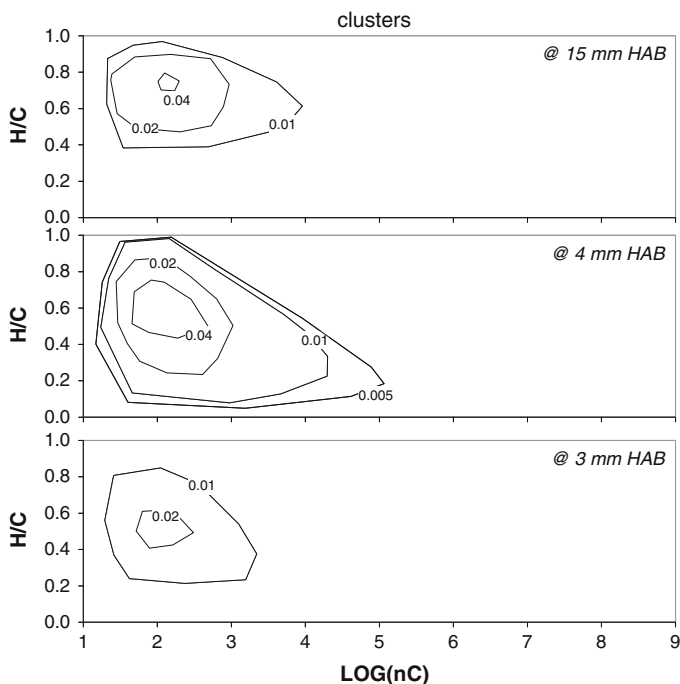


Fig. 14.7 Modeled H/C ratio distribution of clusters as a function of the C-atom numbers (nC) at three heights in the $\phi = 2.4$ flame. From *bottom to top*: 3, 4, and 15 mm. *Lines* are iso-concentrations in part per million (D'Anna et al. 2010, Copyright Elsevier)

where particulate concentration starts to increase quickly (at about 4 mm in Fig. 14.6). Thereafter, the molecular weight and the H/C of molecules remain unchanged with only slight variation toward smaller mass and larger H/C ratio moving into the post-flame region. The number of C-atoms in the molecules does not change dramatically in the various flame regions. Just a slight increase is found moving from the flame front to the post-flame region. This result is consistent with experimental findings which have shown hardly any appreciable increase of the molecular weight of aromatics along the flame axis.

Clusters show a different behavior along the flame axis as shown in Fig. 14.7. They are mainly formed by the molecules with the lowest H/C ratio since these molecules have larger aromatic character and exhibit larger binding energies resulting in increased coagulation efficiency. Figure 14.7 clearly shows that clusters reach masses generally larger than molecules. They start at the flame front with about 50 C-atoms, which correspond to a molecular mass of the order of 1,000 amu and a size of 1.5–2 nm (for unit density and a spherical form). The H/C ratios of these clusters reach values as low as 0.25. At the height where cluster concentration starts to increase quickly (at about 4 mm), larger masses and lower H/C ratio particles are formed. Here the C-atom numbers reach values as large as

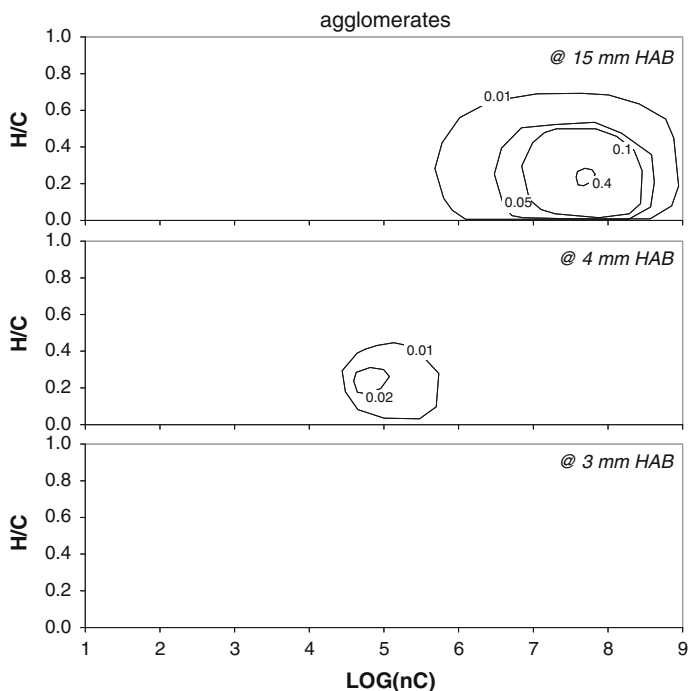


Fig. 14.8 Modeled H/C ratio distribution of agglomerates as a function of the C-atom numbers (nC) at three heights in the $\phi = 2.4$ flame. From *bottom* to *top*: 3, 4, and 15 mm. Lines are iso-concentrations in part per million (D'Anna et al. 2010, Copyright Elsevier)

1×10^5 and H/C as low as 0.1. These clusters can be considered to be the first soot particles. Thereafter, isolated particles show a reduction in mass and an increase in H/C ratios.

The formation of agglomerates is observed with the increase in C-atom number and the decrease in H/C ratio of the particles, as shown in Fig. 14.8. Agglomerates of particles represent the passage from the coalescence to the agglomeration process. The first entities belonging to this class of compounds are detected at the height where particulate concentration starts to increase quickly and they have about 5×10^4 C-atoms and an H/C of 0.25. Moving downstream from the flame front the number of C-atoms of the agglomerates increases to between 1×10^6 and 1×10^9 (equivalent spherical sizes of 30–300 nm) and H/C ratio decreases to 0.05.

The picture of mass grow described by the model is consistent with the C-atom distributions of particulates obtained by Ciajolo and coworkers sampling in flames and analyzing by size exclusion chromatography (SEC) (as shown in Chap. 13), the sampled material (Apicella et al. 2003). Figure 14.9 shows a comparison of the model to the experimentally determined mass distributions of total particulate at inception and in the post-flame region.

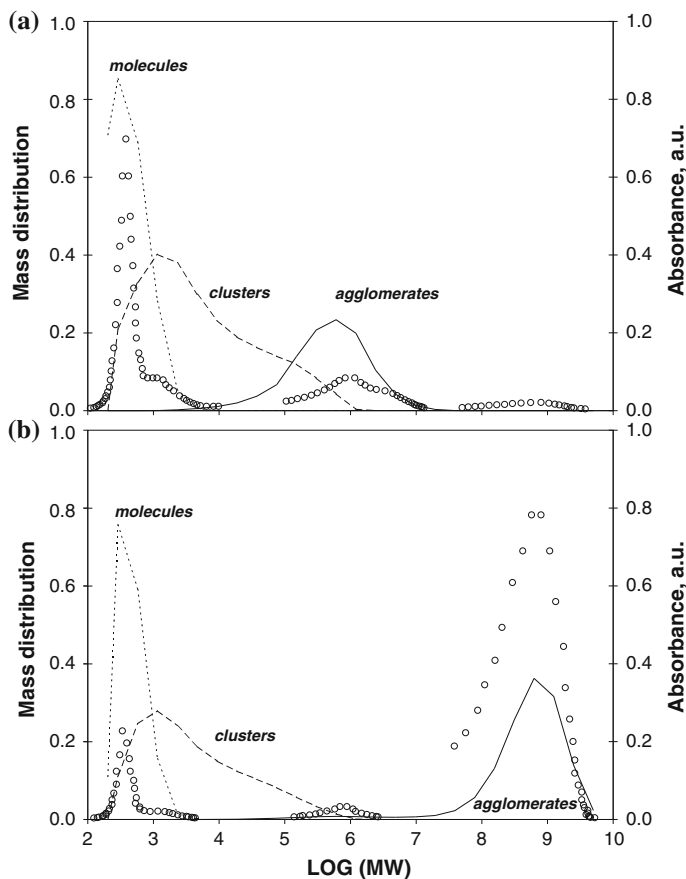


Fig. 14.9 Comparison of the model (lines—Sirignano et al. 2011) with the experimentally determined (points—Apicella et al. 2003) mass distributions of total particulate at (a) inception and (b) in the post-flame region. Mass distributions of total particulate are measured by size exclusion chromatography with absorption detection at 350 nm and normalized for accounting the relative contributions of soot and condensed hydrocarbon species (D’Anna et al. 2010, Copyright Elsevier)

Mass distributions of total particulate are measured by SEC with absorption at 350 nm and are normalized for the relative contributions of soot and condensed hydrocarbon species. Modeled results, instead, represent the concentrations of the different classes of compounds. Although a quantitative comparison cannot be made, the qualitative comparison gives a better understanding of the role of the different classes of compounds in the particulate formation process.

SEC mass distributions in Fig. 14.9 show four mass peaks: species with masses in the range 128–800, 800–5,000, 10^5 – 10^7 and 10^8 – 10^{10} amu. The model shows that the first peak is due to molecules of aromatic compounds having masses up to

2,000 amu. The second peak is due to particles with masses extending up to about 1×10^5 amu. The third peak is due to both particles with masses extending up to about 1×10^6 amu and agglomerates of particles. The fourth peak is due only to agglomerates of particles.

The abundance of the four mass species changes along the flame. At particle inception the first three mass peaks are observed, that is, the molecules of aromatic hydrocarbons, the isolated particles of 2 and 8 nm, and agglomerates of small particles. In the post-flame region the peaks due to the nascent particles are less evident being obscured by the presence of agglomerates of large particles. The model predictions are in agreement with experimental data and help the understanding of the chemical and physical nature of the detected substances.

The model is also applied to explore the effect of equivalence ratio on the formation of particulates. Figure 14.10 shows the comparison of the model to the experimentally determined volume fraction of total particulates at 12 mm height in several premixed flames of ethylene/air with equivalence ratios ranging from 1.5 to 2.5. Total particulate concentrations are determined by absorption measurements in the UV. The particulates comprise all of the carbonaceous species which have an appreciable absorption in the ultraviolet region (D'Alessio et al. 1998). Experimental volume fractions of nanoparticles with sizes larger than 1.5 nm and soot particles are also shown. Nanoparticles were detected by differential mobility analysis or DMA, whereas soot particles were detected by laser-induced incandescence (LII) as described in Chap. 12 and visible absorption (Sgro et al. 2009).

The concentration of total particulate determined by UV absorption increases at increasing equivalence ratios by about two orders of magnitude; the simulation predicts the trend well. It fails to reproduce the concentration of particulate at equivalence ratios close to the stoichiometric value, that is, below 1.6. However, here the error in the UV absorption can become very large due to the interference by gaseous stable species such as H_2O and CO_2 (Joutsenoja et al. 2001).

Model results (Fig. 14.10) show that different equivalence ratio thresholds exist for the types of compounds formed in flames. The onset of molecular compounds occurs at an equivalence ratio of 1.6 in reasonable agreement with the threshold of total particulate determined by UV absorption. Clusters are instead formed at equivalence ratios larger than 1.7. The concentration of the modeled clusters at different equivalence ratios agrees quite well with the concentration of particles detected by DMA which is very sensitive to nanoparticles but not to molecules. Modeled agglomerates of particles start to form at about 2.15. This is in excellent agreement with the threshold of soot particles determined by light absorption in the visible and by LII.

14.4.2 Laminar Diffusion Flames: Test Cases

The non-premixed, co-flowing nonsmoking ethylene/air flame of Santoro and co-workers (Santoro et al. 1983; Santoro and Semerjian 1984; Smyth et al. 1985;

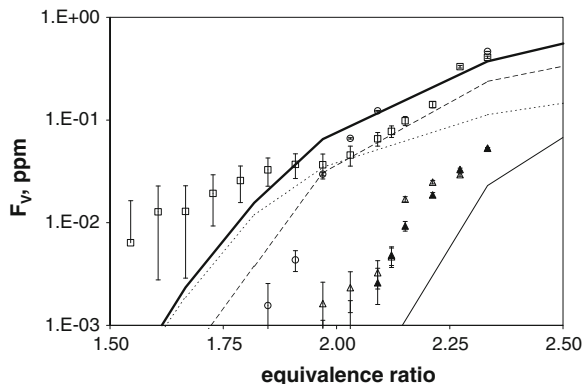


Fig. 14.10 Comparison of the model with the experimentally determined concentrations of total particulate and the different species structures at 12 mm height on the flame axis of several premixed flames of ethylene/air with equivalence ratios ranging from 1.5 to 2.5. Model results: molecules (*point line*), clusters (*dashed line*), agglomerates (*thin continuous line*), and total particulate (*thick continuous line*). Experimental data: total particulate from UV-Vis absorption (□), nanoparticles from DMA (○), soot aggregates from LII (▲), and from visible absorption (△). Experimental data from Ciajolo et al. (1996) and Sgro et al. (2009) (D’Anna et al. 2010, Copyright Elsevier)

Santoro et al. 1987) has also been modeled. Figure 14.11 shows the comparison between predicted and measured temperature and species for this flame. Temperature, ethylene, acetylene, and benzene profiles are shown at 20 and 30 mm above the nozzle. The temperatures and the fuel concentration are well represented by the model at all heights. Benzene and acetylene predictions are somewhat high in the lower part of the flame and do not show the measured decay of these species at 30 mm height.

Radial profiles of particulate volume fractions are shown on the left side of Fig. 14.12 at measurement heights, 20, 30, 60, and 70 mm above the nozzle. The model gives good predictions of soot volume fractions and in particular reproduces the observed burnout of particles at 70 mm.

Particle size D₆₃ is shown on the right side of Fig. 14.12 at the same heights. The model responds well to the heavily sooting fuel by generally representing the measured sizes of the particles.

Figure 14.12 reports as dashed lines the model predictions without particle fragmentation by oxidation. Oxidation-induced fragmentation, which is in parallel with surface oxidation, reduces particle size thereby increasing number concentration and also the rate of oxidation. The inclusion of oxidation-induced fragmentation pathways has improved model accuracy relative to our previous work (D’Anna and Kent 2008) to predict particle size and complete particle burn-out. Complete soot burn-out is now evident with the oxidation-induced fragmentation.

The model correctly reproduces soot concentrations in the wings; mean particle sizes are also well reproduced: maximum particle size is of the order of 100–150 nm compared with about 500–600 nm without fragmentation. D₆₃

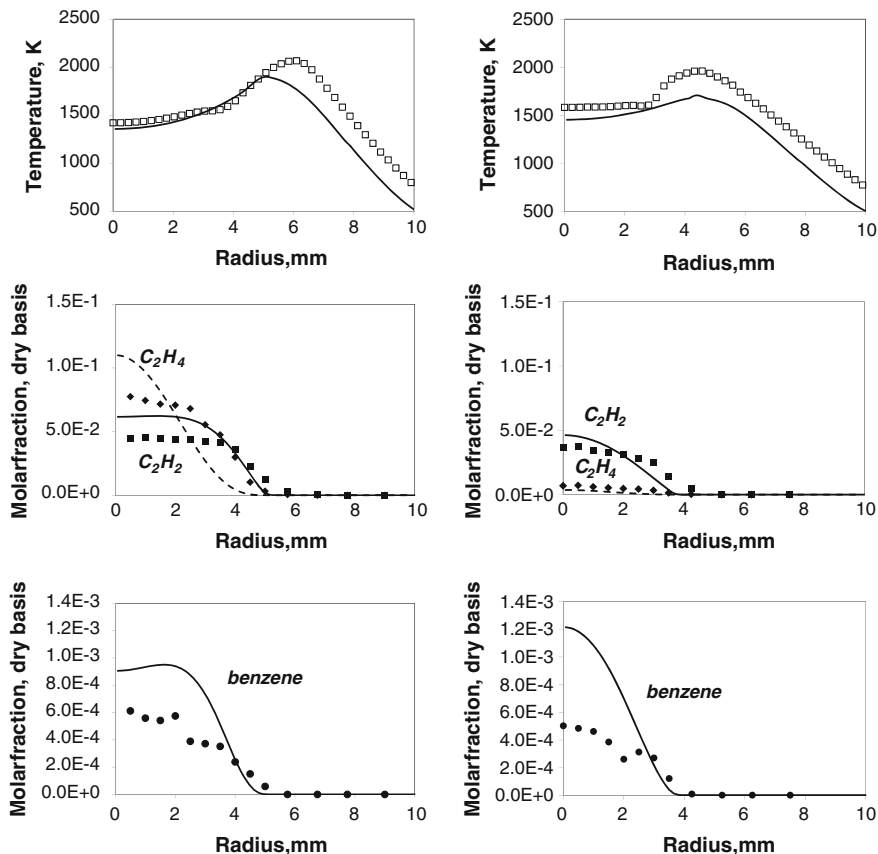


Fig. 14.11 Predicted (*lines*) and measured (*points*) temperature and species radial profiles in non-premixed ethylene co-flowing flame. *Left* 20 mm height, *right* 30 mm height. Experimental data from Santoro group (Santoro et al 1983, 1987). Temperature (\square , $_$); ethylene (\blacklozenge , $---$); acetylene (\blacksquare , $_$); benzene (\bullet , $_$)

modeled data without the oxidation-induced fragmentation are divided by 3 in the figure.

The H-to-C ratio of the particulate collected along the flame axis was measured by Dobbins et al. (1998). The discrimination between C and H in the model allows us to calculate the H/C in the diffusion flame.

Figure 14.13 shows the comparison between measured and calculated H/C along the axis of the nonsmoking ethylene flame. Particles have been extracted from selected heights of the non-premixed coflowing ethylene flame using thermophoretic sampling and chemically analyzed by laser microprobe mass spectroscopy. Model follows the trend of the H/C ratio; it shows values of the order of 0.6, typical of PAHs, close to the burner mouth. Thereafter at about 20 mm, it sharply decreases to values of the order of 0.2 when soot formation starts also on

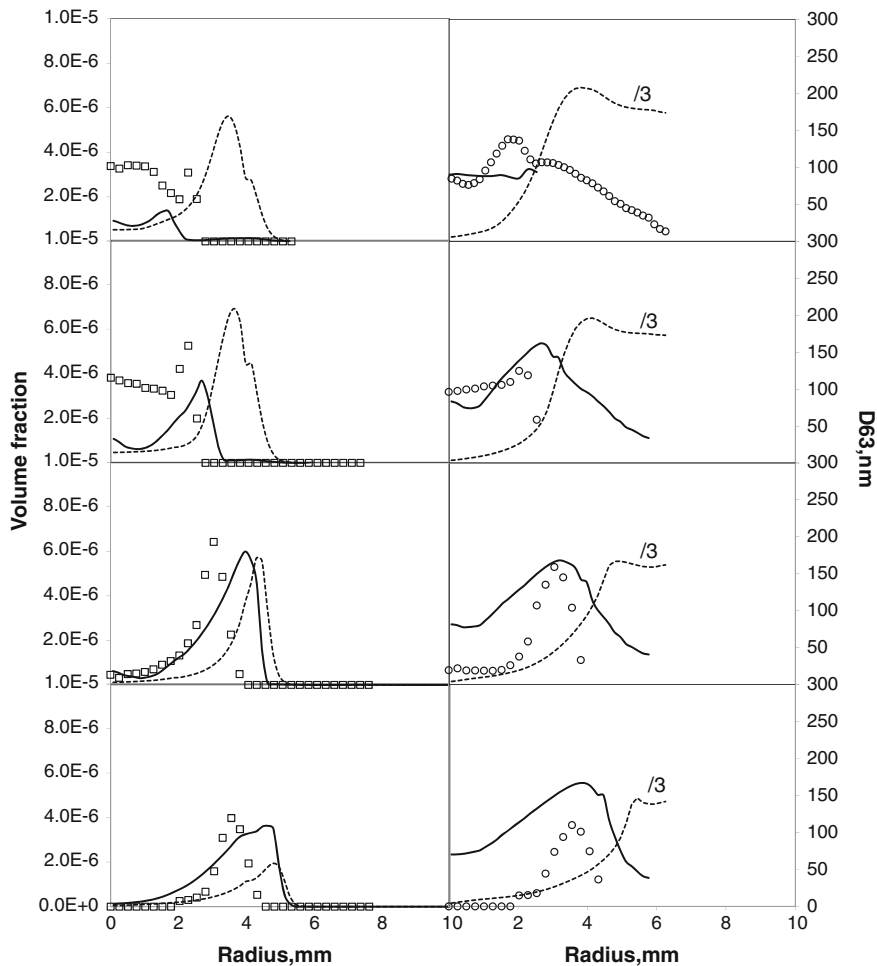
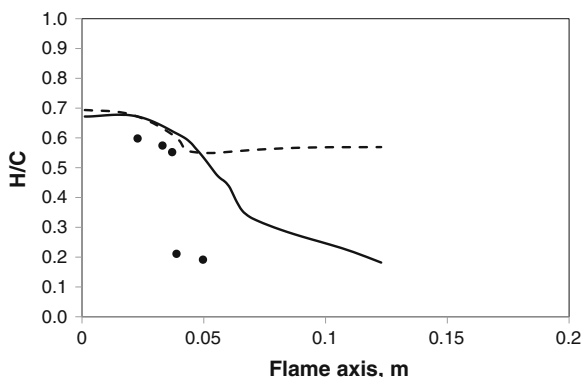


Fig. 14.12 Total particulate volume fraction (*left*) and mean particle size (*right*) profiles in non-premixed ethylene co-flowing flame. From *bottom* to *top* radial profiles at 20, 30, 60, and 70 mm height. Volume fraction data by laser-induced incandescence (Santoro et al. 1983, 1987). D63 data by scattering and extinction (Santoro et al. 1983, 1987). Modeled data: *continuous lines* represents results of the complete mechanism, *dashed lines* represents results of the mechanism without particle fragmentation induced by oxidation

the flame axis. The model does not predict the correct height where H-to-C ratio decreases, whereas the overall prediction of the aromatization process is matched. Figure 14.12 also shows the H/C profile obtained without taking into account the dehydrogenation pathway showing the importance of this mechanism in correctly reproducing the behaviors of particulate matter in flames.

Fig. 14.13 Comparison of predicted H/C along the flame axis of non-premixed ethylene flame (*lines*) with experimental data (*points*) from Dobbins et al. (1998)



14.5 Final Remarks

The latest version of a multi-sectional kinetic mechanism of aromatic growth and particulate formation is presented and it is tested over a range of different operating conditions in rich premixed and non-premixed flames of ethylene. The kinetic model has been built-up and refined by comparing model predictions with experimental data on the formation of high-molecular mass species and particles. Good predictions are obtained of major oxidation and pyrolysis products, as well as of trace species and particle concentrations and size distributions. The model is able to predict premixed and non-premixed flames of ethylene at atmospheric pressure without any adjustments to the scheme.

The model predicts a wide range of particle sizes. Particles with sizes below 10 nm having a modal diameter of about 2 nm are formed in premixed flames below the soot formation threshold and in the fuel side of non-premixed flames, in good agreement with the concentration of condensed hydrocarbon species and nanoparticle of organic carbon (NOC) experimentally detected by various techniques. The model predicts also the H/C ratios of these nanoparticles well in both premixed and non-premixed conditions.

Sensitivity of the predictions to the particulate-phase reaction rates has been performed showing the importance of the modeling of soot particle oxidation for the correct prediction of particle concentrations and sizes. In particular, the mechanism of oxidation-induced fragmentation allows the predictions of the right sizes of the particles and the complete burn-out in non-premixed conditions.

References

- Alfè M, Apicella B, Barbella R et al (2009) Structure–property relationship in nanostructures of young and mature soot in premixed flames. *Proc Combust Inst* 32:697–704
- Apicella B, Ciajolo A, Barella R et al (2003) Size exclusion chromatography of particulate produced in fuel-rich combustion of different fuels. *Energy Fuels* 17:565–570

- Ciajolo A, D'Anna A, Barbella R et al (1996) The effect of temperature on soot inception in premixed ethylene flames. *Symp (Int) Combust* 26:2327–2333
- Ciajolo A, Barbella R, Tregrossi A et al (1998) Spectroscopic and compositional signatures of PAH-loaded mixtures in the soot inception region of a premixed ethylene flame. *Symp (Int) Combust* 27:1481–1487
- D'Alessio A, D'Anna A, Gambi G et al (1998) The spectroscopic characterization of UV absorbing nanoparticles in fuel rich soot forming flames. *J Aerosol Sci* 29:397–409
- D'Alessio A, Barone AC, Cau R et al (2005) Surface deposition and coagulation efficiency of combustion generated nanoparticles in the size range from 1 nm to 10 nm. *Proc Combust Inst* 30:2595–2603
- D'Anna A (2009a) Combustion-formed nanoparticles. *Proc Combust Inst* 32:593–613
- D'Anna A (2009b) Particle inception and growth: experimental evidences and a modelling attempt. In: Bockhorn H, D'Anna A, Sarofim AF, Wang H (eds) *Combustion generated fine carbonaceous particles*. Karlsruhe University Press, Karlsruhe, pp 289–320
- D'Anna A, Kent JH (2008) A model of particulate and species formation applied to laminar, nonpremixed flames for three aliphatic-hydrocarbon fuels. *Combust Flame* 152:573–587
- D'Anna A, Sirignano M, Kent JH (2010) A model of particle nucleation in premixed ethylene flames. *Combust Flame* 157:2106–2115
- Dobbins RA, Fletcher RA, Chang H-C (1998) The evolution of soot precursor particles in a diffusion flame. *Combust Flame* 115:285–298
- Dworkin SB, Zhang Q, Thomson MJ et al (2011) Application of an enhanced PAH growth model to soot formation in a laminar coflow ethylene/air diffusion flame. *Combust Flame* 158:1682–1695
- Echavarria CA, Jaramillo IC, Sarofim AF et al (2011) Studies of soot oxidation and fragmentation in a two-stage burner under fuel-lean and fuel-rich conditions. *Proc Combust Inst* 33:659–666
- Frenklach M, Wang H (1991) Detailed modeling of soot particle nucleation and growth. *Symp (Int) Combust* 23:1559–1566
- Frenklach M, Wang H (1994) Detailed mechanism and modeling of soot particle formation. In: Bockhorn H (ed) *Soot formation in combustion: mechanisms and models*, Springer series in chemical physics 59. Springer-Verlag, Heidelberg, pp 165–192
- Hamaker HC (1937) The London–van der Waals attraction between spherical particles. *Physica* 4:1058–1072
- Homann K-H (1998) Fullerenes and soot formation new pathways to large particles in flames. *Angew Chem Int Ed* 37:2434–2451
- Joutsenoja T, D'Anna A, D'Alessio A et al (2001) Ultraviolet absorption spectra of carbon dioxide and oxygen at elevated temperatures. *Appl Spect* 55:130–135
- Kazakov A, Frenklach M (1998) Dynamic modeling of soot particle coagulation and aggregation: implementation with the method of moments and application to high-pressure laminar premixed flames. *Combust Flame* 114:484–510
- Marinov NM, Pitz WJ, Westbrook CK, Castaldi MJ, Senkan SM (1996) Modeling of aromatic and polycyclic aromatic hydrocarbon formation in premixed methane and ethane flames. *Combust Sci Technol* 116–117:211–287
- Mauss F, Netzell K, Marchal C et al (2009) Modeling the soot particle size distribution functions using a detailed kinetic soot model and a sectional method. In: Bockhorn H, D'Anna A, Sarofim AF, Wang H (eds) *Combustion generated fine carbonaceous particles*. Karlsruhe University Press, Karlsruhe, pp 465–482
- Miller JA, Melius CF (1992) Kinetic and thermodynamic issues in the formation of aromatic compounds in flames of aliphatic fuels. *Combust Flame* 91:21–39
- Mueller ME, Blanquart G, Pitsch H (2011) Modeling the oxidation-induced fragmentation of soot aggregates in laminar flames. *Proc Combust Inst* 33:667–674
- Neoh KG, Howard JB, Sarofim AF (1985) Effect of oxidation on the of soot. *Symp (Int) Combust* 20:951–957

- Richter H, Granata S, Green WH et al (2005) Detailed modeling of PAH and soot formation in a laminar premixed benzene/oxygen/argon low-pressure flame. *Proc Combust Inst* 30:1397–1405
- Russo C, Alfè M, Rouzaud J-N et al (2013) Probing structures of soot formed in premixed flames of methane, ethylene and benzene. *Proc Combust Inst* 34:1885–1892
- Santoro RJ, Semerjian HG, Dobbins RA (1983) Soot particle measurements in diffusion flames. *Combust Flame* 51:203–218
- Santoro RJ, Semerjian HG (1984) Soot formation in diffusion flames: flow rate, fuel species, and temperature effects. *Symp (Int) Combust* 20:997–1006
- Santoro RJ, Yeh TT, Horvath JJ et al (1987) The transport and growth of soot particles in laminar diffusion flames. *Combust Sci Technol* 53:89–115
- Sgro LA, Barone AC, Commodo M et al (2009) Measurement of nanoparticles of organic carbon in non-sooting flame conditions. *Proc Combust Inst* 32:689–696
- Sirignano M, Kent JH, D'Anna A (2010) Detailed modeling of size distribution functions and hydrogen content in combustion-formed particles. *Combust Flame* 157:1211–1219
- Sirignano M, Alfè M, Tregrossi A et al (2011) Experimental and modeling study on the molecular weight distribution and properties of carbon particles in premixed sooting flames. *Proc Combust Inst* 33:633–640
- Smith GP, Golden DM, Frenklach M et al (2013). http://www.me.berkeley.edu/gri_mech/
- Smooke MD, McEnally CS, Pfefferle LD (1999) Computational and experimental study of soot formation in a coflow, laminar diffusion flame. *Combust Flame* 117:117–139
- Smyth KC, Miller JH, Dorfman RC et al (1985) Soot inception in a methane/air diffusion flame as characterized by detailed species profiles. *Combust Flame* 62:157–181
- Xu F, El-Leathy AM, Kim CH et al (2003) Soot surface oxidation in hydrocarbon/air diffusion flames at atmospheric pressure. *Combust Flame* 132:43–57